

Electrostatically confined Quantum Rings in bilayer Graphene

M. Zarenia¹, J. M. Pereira Jr.², F. M. Peeters^{1,2}, and G. A. Farias²

¹*Department of Physics, University of Antwerp, Groenenborgerlaan 171, B-2020 Antwerpen, Belgium*

²*Departamento de Física, Universidade Federal do Ceará, Fortaleza, Ceará, 60455-760, Brazil.*

We propose a new system where electron and hole states are electrostatically confined into a quantum ring in bilayer graphene. These structures can be created by tuning the gap of the graphene bilayer using nanostructured gates or by position-dependent doping. The energy levels have a magnetic field (B_0) dependence that is strikingly distinct from that of usual semiconductor quantum rings. In particular, the eigenvalues are not invariant under a $B_0 \rightarrow -B_0$ transformation and, for a fixed total angular momentum index m , their field dependence is not parabolic, but displays two minima separated by a saddle point. The spectra also display several anti-crossings, which arise due to the overlap of gate-confined and magnetically-confined states.

PACS numbers: 71.10.Pm, 73.21.-b, 81.05.Uw

The electronic properties of low-dimensional systems have long been an area of intense research. In recent years, a particularly interesting two-dimensional (2D) system, namely single layers of crystal carbon (graphene), has been obtained experimentally. The striking mechanical and electronic properties of graphene have quickly been recognized and promise to lead to new applications in electronic devices and sensors. These devices will benefit from the large charge carrier mobilities and long mean free paths at room temperature^{1,2,3,4,5}. It has been recognized that two coupled layers of graphene (bilayer graphene - BG) is a very different material from graphene and also from graphite. The carrier spectrum of electrons in ideal BG is gapless and approximately parabolic at low energies around two points in the Brillouin zone (\mathbf{K} and \mathbf{K}')^{6,7}. In the presence of a perpendicular electric field, however, the spectrum is found to display a gap, which can be tuned by varying the bias, or by chemical doping of the surface⁸. This tunable gap can then be exploited for the development of BG devices. In particular, the possibility of tailoring the energy gap in BG has raised the prospect of the creation of electrostatically defined quantum dots in bilayer graphene by means of a position-dependent doping or through the deposition of split gates on the BG surface⁹.

A very important class of quantum devices consists of quantum rings. They have generated a lot of interest, especially because they allow the observation of quantum phase coherence effects on carrier transport such as in the Aharonov-Bohm¹⁰ and Aharonov-Casher¹¹ effects. Semiconductor-based quantum rings have been obtained experimentally¹² and, recently, quantum rings have also been studied on single-layer graphene, both theoretically and experimentally^{13,14}. The latter have been produced by lithographic techniques in which graphene nanoribbons or ring structures are carved from an otherwise defect-free surface. Such techniques permit the production of devices in the nanometer scale, but have the disadvantage of creating defects at the edges of the graphene-based structure which may reduce the overall performance, as well as raise difficulties for the theoretical analysis of the device. These quantum rings can also

be described as graphene flakes with a central antidot, and recent calculations indicate that localized edge states strongly affect the spectrum of these systems¹⁵. Additionally, the specific type of edge (zig-zag versus arm-chair) was also found to influence their electronic properties.

To overcome the problems related to the edges of the quantum ring (i.e. defects and type of edge) we propose here an electrostatically defined graphene-based quantum ring (GQR). In contrast with previous quantum rings on graphene, the system considered here is created by the use of electrostatic potentials which induce a position-dependent gap, such that the low-energy electron and hole states can be confined in a ring-shaped region of an otherwise ideal BG sheet. This type of confinement is not possible in single layer graphene, due to the Klein tunneling effect¹⁶. In our proposed structure, the effects of the edges are not relevant since the BG sheet is assumed to be defect-free and the confinement is brought about by an external bias. Moreover, in contrast with structures carved by means of lithography, the ring parameters can be tuned by external fields, a feature that can be particularly relevant for the design of field configurable devices. Here, we obtain the energy levels and wavefunctions of the confined electron and hole states by numerically solving the Dirac equation and results are presented as function of ring radius, width and magnetic field.

Bilayer graphene consists of two weakly, van der Waals coupled honeycomb sheets of covalent-bond carbon atoms in a Bernal AB stacking. The system can be described in terms of four sublattices, labelled A, B (upper layer) and C, D (lower layer). The A and C sites are coupled via a nearest-neighbor interlayer hopping term t . We employ the continuum model based on the Dirac equation, which is known to provide a realistic description of graphene-based structures with dimensions that are much larger than the lattice parameter and that has been shown to give good agreement with experimental data.

The Hamiltonian, in the vicinity of the \mathbf{K} valley and in the presence of a magnetic field normal to the plane

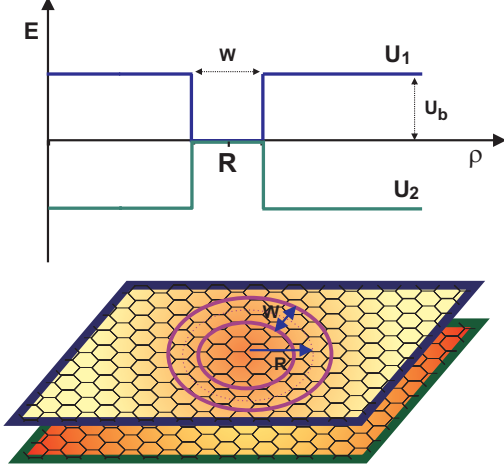


FIG. 1: Schematic depiction of the potential profile for a bilayer graphene quantum ring

of the layer is given by⁸

$$\mathcal{H} = \begin{pmatrix} U_0 + \frac{\Delta U}{2} & \pi & t & 0 \\ \pi^\dagger & U_0 + \frac{\Delta U}{2} & 0 & 0 \\ t & 0 & U_0 - \frac{\Delta U}{2} & \pi^\dagger \\ 0 & 0 & \pi & U_0 - \frac{\Delta U}{2} \end{pmatrix}, \quad (1)$$

where $t \approx 400$ meV is the interlayer coupling term, $\pi = v_F[(p_x + eA_x) + i(p_y + eA_y)]$, \mathbf{p} is the momentum operator, \mathbf{A} is the vector potential, $\Delta U = U_1 - U_2$ is the difference of potential between the layers, $U_0 = (U_1 + U_2)/2$ is the average potential, and $v_F \approx 1 \times 10^6$ m/s is the Fermi velocity. In this work we neglect the small Zeeman splitting of the energy levels.

The eigenstates of Eq. (1) are four-component spinors $\Psi = [\psi_A, \psi_B, \psi_C, \psi_D]^T$, where ψ_i ($j = A, B, C, D$) are the envelope functions associated with the probability amplitudes at the respective sublattice sites of the upper and lower graphene sheets. For a circular-symmetric, position-dependent potential such as the one described in Ref. [9], the spinor components are $\psi_A = \phi_A(\rho)e^{im\theta}$, $\psi_B = \phi_B(\rho)e^{i(m-1)\theta}$, $\psi_C = \phi_C(\rho)e^{im\theta}$, and $\psi_D = \phi_D(\rho)e^{i(m+1)\theta}$, where m is the angular momentum label. Using the symmetric gauge $\mathbf{A} = (0, B_0\rho/2, 0)$, the radial dependence of the spinor components is described, in dimensionless units, by

$$\begin{aligned} \left[\frac{d}{dr'} + \frac{m}{r'} + \beta r' \right] \phi_A &= -(\alpha - \delta) \phi_B, \\ \left[\frac{d}{dr'} - \frac{(m-1)}{r'} - \beta r' \right] \phi_B &= (\alpha - \delta) \phi_A + t' \phi_C, \\ \left[\frac{d}{dr'} + \frac{(m+1)}{r'} + \beta r' \right] \phi_D &= (\alpha + \delta) \phi_C + t' \phi_A, \\ \left[\frac{d}{dr'} - \frac{m}{r'} - \beta r' \right] \phi_C &= -(\alpha + \delta) \phi_D, \end{aligned} \quad (2)$$

where $r' = \rho/R$, $\alpha = \epsilon - u_0$, $u_0 = (u_1 + u_2)/2$, and

$\delta = \Delta u/2$, with $\Delta u = u_1 - u_2$. The energy, the potentials and the interlayer coupling strength are written in dimensionless units as $\epsilon = E/E_0$, $u_{1,2} = U_{1,2}/E_0$, $t' = t/E_0$ and $E_0 = \hbar v_F/R$, where ρ is the radial variable and R is the ring radius. The dimensionless parameter $\beta = (eB/2\hbar)R^2$, can be expressed as Φ/Φ_0 , where Φ is the magnetic flux threading the ring and $\Phi_0 = h/e$ is the quantum of magnetic flux.

In this paper we solve Eq. (2) by the finite elements method for the following profile (see Fig. 1) :

$$\delta = \begin{cases} 0 & 1 - \frac{w'}{2} \leq r' < 1 + \frac{w'}{2} \\ u_b & 0 < r' < 1 - \frac{w'}{2}, \quad 1 + \frac{w'}{2} \leq r' < \infty \end{cases} \quad (3)$$

where $w' = W/R$, with W being the width of the ring. This potential describes a bilayer graphene quantum ring (GQR) of radius R and width W , in which both electron and holes are confined by a tunable potential barrier U_b . As shown in Ref. [9], the wavefunctions given by Eq. (2) are eigenstates of the operator

$$J_z = L_z + \frac{\hbar}{2} \begin{pmatrix} -\mathbf{I} & 0 \\ 0 & \mathbf{I} \end{pmatrix} + \frac{\hbar}{2} \begin{pmatrix} \sigma_z & 0 \\ 0 & -\sigma_z \end{pmatrix} \quad (4)$$

with eigenvalue m , where \mathbf{I} is the 2×2 identity matrix, L_z is the angular momentum operator and σ_z is one of the Pauli matrices. The above equation can be rewritten as $J_z = L_z + \hbar\tau_z + \hbar S_z$, where the second term in the right hand side is a layer index operator, which is associated with the behavior of the system under inversion, whereas S_z carries the information on the pseudospin components in each layer. It should be emphasized that in this system, L_z does not commute with the Hamiltonian and is no longer quantized.

Figure 2 shows the lowest energy levels of a GQR as function of ring radius R (upper panel), and width W (lower panels), for $m = -1$ (a,d), $m = 0$ (b,e), and $m = 1$ (c,f), for $W = 20$ nm (a-c), $R = 50$ nm (d-f), $U_b = 150$ meV and $B = 0$. The results show a weak dependence on the ring radius and an interesting electron-hole asymmetry, which is due to the breaking of the inversion symmetry by the external bias. However, the electron and hole energy levels are invariant under the transformation $E(m) \rightarrow -E(-m)$. In Fig. 3, the lowest energy levels of a QR are shown as function of ring radius in the presence of a non-zero magnetic field, $B_0 = 5$ T, for $-3 \leq m \leq 3$, $W = 20$ nm and $U_b = 150$ meV. In contrast with the zero field case, the results show a strong dependence on the ring radius, with the appearance of several crossings, as shown more clearly in the inset.

The energy levels of electrons and holes for the \mathbf{K} valley in a GQR are presented in Fig. 4 as function of external magnetic field B_0 , for $-10 \leq m \leq -1$ (red curves), $m = 0$ (green curves) and $1 \leq m \leq 10$ (blue curves) with $R = 50$ nm, $W = 20$ nm and $U_b = 150$ meV. In contrast with the results obtained from the Schrödinger equation, the spectra are not invariant under the transformation $B_0 \rightarrow -B_0$. Moreover, the individual branches display two local minima. The figures also show a set of

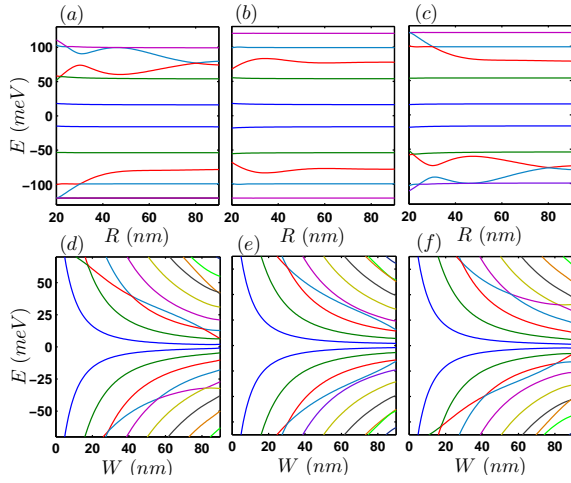


FIG. 2: Lowest energy levels of a graphene bilayer quantum ring as function of ring radius R (Panels: a, b, c) and width of the ring W (d, e, f). Parameters given in the text.

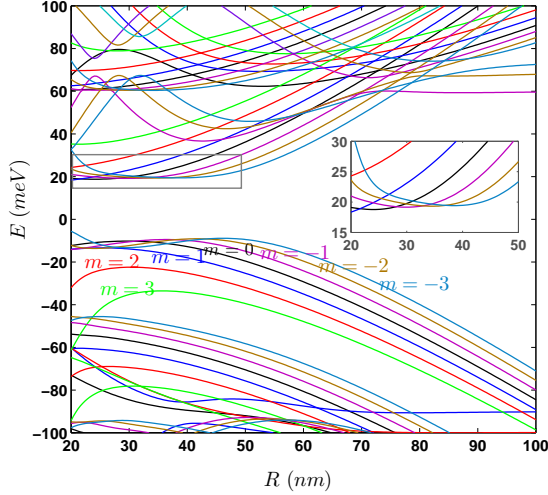


FIG. 3: Energy levels of a bilayer graphene quantum ring as function of ring radius R . Parameters given in the text.

branches with energies that decay as the field increases. These states correspond to Landau levels of the biased bilayer, for which the carrier confinement is mainly due to the magnetic field. By making a small gap in the confinement region of the ring it can be evidenced that those branches are only weakly affected by a variation of the gap. We found that the electron and hole energies are related by $E_e(m, B_0) = -E_h(-m, -B_0)$. The spectrum for the \mathbf{K}' valley can be obtained by setting $B_0 \rightarrow -B_0$, which shows that, as in the case of the graphene bilayer quantum dot⁹, the valley degeneracy is lifted. The four lower panels show the probability density of the points on the spectrum which are labeled by (a), (b), ... in the upper panel. The vertical dashed lines indicate the edges

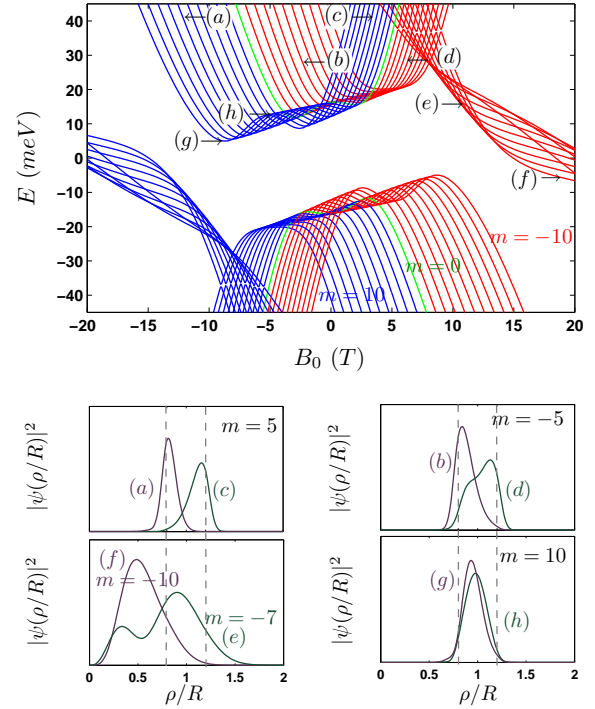


FIG. 4: Electron and hole energy states of a graphene bilayer ring-shaped quantum dot as function of external magnetic field B_0 . Parameters given in the text.

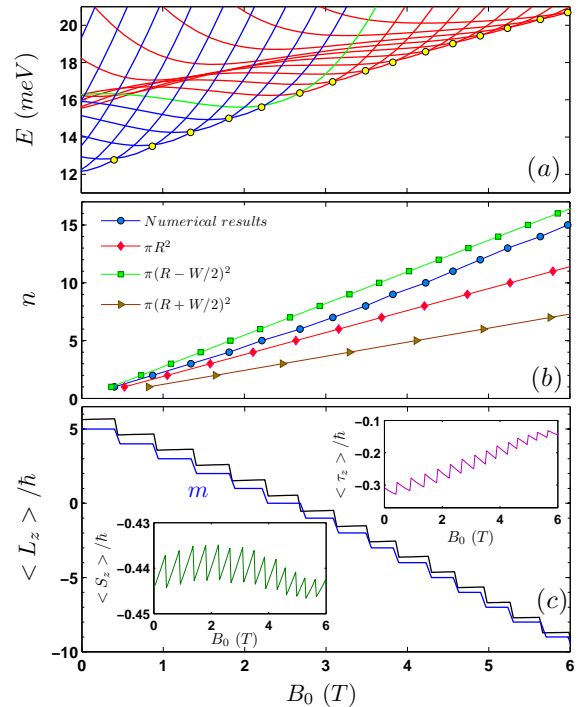


FIG. 5: (a) Enlargement of the electron spectrum of Fig (4). (b) Number of transitions between the levels (circles) and AB oscillations for a ring with radius R and surface $S = \pi R^2$, $S = \pi(R \pm W/2)^2$. (c) Ground state expectation values of L_z/\hbar , τ_z/\hbar and S_z/\hbar as function of the magnetic field.

of the ring. As seen, for the (e) and (f) points the probability density has peaks in the internal region of the ring structure ($\rho < R - W/2$), whereas for the remaining points the carriers are mainly confined inside the ring. The (e) and (f) states belong to energy states that in the limit $B_0 \rightarrow \infty$ approach the zero Landau level are shifted from $E = 0$ due to the presence of the ring potential. An enlargement of the region of the spectrum is shown in Fig. 5(a). The yellow dots correspond to the location of the transitions of the ground state between the levels which is related to the number of AB oscillations $n = \Phi/\Phi_0$. Figure 5(b) shows the number of transitions between the levels (circles) and the AB oscillations for a zero-width ring with radius R and surface $S = \pi R^2, S = \pi(R \pm W/2)^2$. Notice that the numerical results obtained for the finite width ring follow closely the AB oscillations as expected for an ideal ring with radius equal to the one of the inner ring.

The ground state expectation values of the L_z/\hbar , τ_z/\hbar and S_z/\hbar operators are shown as function of the magnetic field in Fig. 5(c). The figure shows that the values of $\langle L_z \rangle / \hbar$ (black curve), $\langle \tau_z \rangle / \hbar$ (upper inset) and $\langle S_z \rangle / \hbar$ (lower inset) are not quantized, but, their sum, as in Eq. (4) (blue curve) is given by the m quantum number. Very different from the Schrödinger case we find that for $B_0 \approx 0$ the quantum number m and the average $\langle L_z \rangle$ are non-zero.

The spectrum in Fig. 4 exhibits several anticrossings between different branches. An enlargement of one particular anticrossing (between the first and second level of $m = -1$) is displayed in Fig. 6(a). The corresponding values of $\langle L_z \rangle$, the average radial position $\langle \rho/R \rangle$, as well as the probability density for the points (1), (2) and (3) are shown in panels (b), (c) and (d), respectively. The figure indicates that at the anti-crossing the eigenstate evolves from a configuration in which the electron is mainly confined in the center of the ring by the magnetic field, to a state in which the confinement is mainly caused by the electrostatic potential U_b . At the anti-crossing (2), the probability density plot shows peaks both in the central part of the structure, as well as in the ring, which characterizes the overlap of the magnetically and electrostatically confined states.

In summary, we obtained the eigenstates and energy levels of electrostatically confined quantum rings in graphene bilayers. This new approach differs from previous studies of graphene-based quantum rings which were realized through a lithographic cutting of the sample. The advantage of the present approach is that the confinement can be tuned by varying the profile and depth of the confining potential, preventing issues as edge disorder and the specific edge type. Numerical results were presented for a step-like confining potential, which can be expected to provide a good approximation of actual potential barriers, because of the large screening in bilayer graphene. We predict that the energy levels display a dependence on the magnetic field that is quite distinct from that of a conventional 2D electron gas. Moreover,

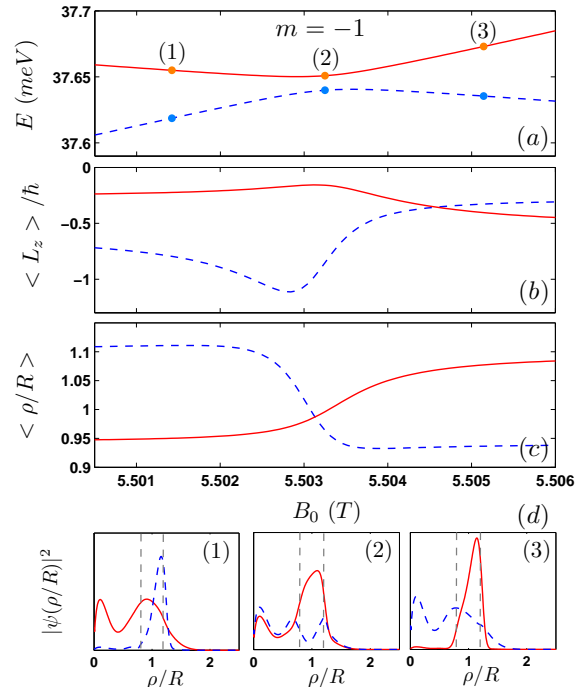


FIG. 6: (a) Enlargement around an anti-crossing point in the energy spectrum. (b) Expectation value of angular momentum $\langle L_z \rangle / \hbar$ and (c) radial average position $\langle \rho/R \rangle$ around the anti-crossing point shown in (a). (d) Probability density for the points (1), (2) and (3) shown in (a).

the energy levels are not invariant under a $B_0 \rightarrow -B_0$ transformation, in contrast with usual ring structures. This is a consequence of the fact that the ring structure is produced by a gate that introduces an electric field and thus a preferential direction. On the other hand, the spectrum is found to be invariant under the transformation $B_0 \rightarrow -B_0$, together with $U_b \rightarrow -U_b$ and $m \rightarrow -m$. Alternatively, $B_0 \rightarrow -B_0$ and $E \rightarrow -E$ transforms electron states into hole states and vice-versa. The spectra also present several anti-crossings at low energies, which arise due to the overlap of gate-confined and magnetically-confined states. For a fixed total angular momentum index m , the $E(B_0)$ curves are no longer parabola, but show two minima separated by a saddle point. The existence of Aharonov-Bohm oscillations for both electrons and holes are still linked with flux quantization through the ring. Throughout the calculation, we considered single electron states. However, the inclusion of Coulomb interaction between carriers may introduce interesting modifications in the spectrum¹⁷. The system can be realized experimentally by a suitable choice of nanostructured doping levels or with the application of nanostructured gates. The spectra may be investigated by, e.g. cyclotron resonance methods¹⁸ and quantum transport measurements.

Acknowledgements. This work was supported by the Flemish Science Foundation (FWO-VI), the Belgian

Science Policy (IAP), the Bilateral program between Flanders and Brazil, and the Brazilian Council for Research (CNPq).

-
- ¹ Y. Zheng and T. Ando, *Phys. Rev. B* **65**, 245420 (2002).
² K. S. Novoselov, A. K. Geim, S. V. Morozov, D. Jiang, Y. Zhang, S. V. Dubonos, I. V. Grigorieva, and A. A. Firsov, *Science*, **306**, 666 (2004).
³ K. S. Novoselov, A. K. Geim, S. V. Morozov, D. Jiang, M. I. Katsnelson, I. V. Grigorieva, S. V. Dubonos, and A. A. Firsov, *Nature (London)* **438**, 197 (2005).
⁴ V. P. Gusynin and S. G. Sharapov, *Phys. Rev. Lett.* **95**, 146801 (2005).
⁵ Y. Zhang, Y. W. Tan, H. L. Stormer, and P. Kim, *Nature (London)* **438**, 201 (2005).
⁶ B. Partoens and F. M. Peeters, *Phys. Rev. B* **74**, 075404 (2006).
⁷ T. Ohta, A. Bostwick, T. Seyller, K. Horn, and E. Rotenberg, *Science* **313**, 951 (2006).
⁸ Edward McCann and Vladimir I. Fal'ko, *Phys. Rev. Lett.* **96**, 086805 (2006).
⁹ J. M. Pereira Jr., P. Vasilopoulos, and F. M. Peeters, *Nano Lett.* **7**, 946, (2007); J. M. Pereira Jr., P. Vasilopoulos, F. M. Peeters, and G. A. Farias, *Phys. Rev. B* **79**, 195403 (2009).
¹⁰ Y. Aharonov and D. Bohm, *Phys. Rev.* **115**, 485 (1959).
¹¹ Y. Aharonov and A. Casher, *Phys. Rev. Lett.* **53**, 319 (1984).
¹² A. Fuhrer, S. Lüscher, T. Ihn, T. Heinzel, K. Ensslin, W. Wegscheider, and M. Bichler, *Nature* **413**, 822 (2001).
¹³ S. Russo, J. B. Oostinga, D. Wehenkel, H. B. Heersche, S. S. Sobhani, L. M. K. Vandersypen, and A. F. Morpurgo, *Phys. Rev. B* **77**, 085413 (2008).
¹⁴ F. Molitor, M. Huefner, A. Jacobsen, A. Pioda, C. Stampfer, K. Ensslin, and T. Ihn, arXiv:0904.1364v1.
¹⁵ D. A. Bahamon, A. L. C. Pereira, and P. A. Schulz, *Phys. Rev. B* **79**, 125414 (2009).
¹⁶ M. I. Katsnelson, K. S. Novoselov, and A. K. Geim *Nature Physics* **2**, 9, 620 (2006); V. V. Cheianov and V. I. Fal'ko, *Phys. Rev. B* **74**, 041403(R) (2006); J. M. Pereira Jr., P. Vasilopoulos, and F. M. Peeters, *Appl. Phys. Lett.* **90**, 132122 (2007).
¹⁷ D. S. L. Abergel, Vadim M. Apalkov, and Tapash Chakraborty, *Phys. Rev. B* **78**, 193405 (2008).
¹⁸ E. A. Henriksen, Z. Jiang, L.-C. Tung, M. E. Schwartz, M. Takita, Y.-J. Wang, P. Kim, and H. L. Stormer, *Phys. Rev. Lett.* **100**, 087403 (2008).